Modeling and Analysis of a Liquid-Cooled Heat Sink for Inverters Used in Hybrid Electric Vehicles

Leonardo Meinerz Abdalla, Paulo Henrique Conrado, Augusto Rodrigues Rauber, Leonardo Roso Colpo, Felipe Bruschi, and Diorge Alex Bao Zambra

***Abstract* - This study presents the experimental characterization and dynamic thermal modeling of a liquid-cooled inverter heatsink for electric vehicle traction applications. The proposed approach considers the entire inverter housing as the heatsink and experimentally validates its thermal behavior under realistic operating conditions. Specifically, the heat transfer system was modeled using a Cauer equivalent circuit. The characterization yielded a thermal resistance of 16.75 m°C/W and a thermal capacitance of 6444.3 J/°C. The model validation was performed on a dynamometer bench with the inverter operating at an input power of 65.86 kW. Under these conditions, the system dissipated 2.34 kW of total power losses, resulting in average IGBT case temperatures of approximately 77 °C. The comparison between the experimental measurements and the model estimates, which predicted a case temperature of 80.48 °C, demonstrates the accuracy and reliability of the developed thermal model for this inverter-heatsink configuration.**

Link to graphical and video abstracts, and to code: https://latamt.ieeer9.org/index.php/transactions/article/view/10417

***Index Terms* – electric vehicles, liquid cooling, traction inverters, thermal modeling.**

I. Introduction

THE growth of the electric vehicle (EV) market has been primarily driven by the need to replace internal combustion engines and mitigate greenhouse gas emissions [1]. Global battery electric vehicle registrations increased from 2.3 million units in 2019 to 17 million units in 2024, corresponding to approximately 15% of the total automotive market [2]. This expansion has intensified the demand for propulsion systems with higher efficiency, reduced volume, and increased power density. In this scenario, the traction inverter plays a central role in overall powertrain performance, as its efficiency, together with the electric machine efficiency map, directly determines how stored electrical energy is converted into mechanical power [3].

Recent inverter developments have focused on increasing power density while simultaneously reducing weight and size [4]. However, these improvements lead to higher thermal stresses on semiconductor devices, whose reliability and lifetime are strongly dependent on junction temperature and thermal cycling conditions [5]. As a result, thermal management has become a critical design constraint in modern automotive traction systems.

Liquid-cooled heatsinks are widely adopted in automotive inverters due to their high heat transfer capability and compact integration potential [6], [7]. The internal geometry, fin configuration, and flow distribution significantly influence heat dissipation performance [8]. In addition, coolant selection plays a fundamental role in ensuring material compatibility, corrosion resistance, and long-term reliability [9], [10]. In specific automotive applications, such as systems in which the stator of a permanent magnet synchronous machine (PMSM) is immersed in coolant and the inverter baseplate is manufactured from aluminum, dielectric oil becomes mandatory despite its lower thermal performance compared to water-based solutions [11]. The increasing adoption of high-power-density PMSMs, particularly axial-flux configurations [12], further reinforces the need for integrated and application-oriented thermal design.

Significant advances in thermal modeling methodologies for electrified automotive systems have been reported in recent years. Structured approaches have been proposed to convert detailed three-dimensional physical models into equivalent thermal networks, enabling computational efficiency while preserving physical consistency [13]. Electro-thermal coupled models have been introduced to predict the junction temperature of SiC MOSFET modules under realistic operating conditions by dynamically linking electrical losses and thermal response [14]. Additional studies have emphasized the strong coupling between temperature-dependent electrical parameters and package-level thermal behavior in high-power automotive MOSFETs [15]. At the cooling system level, experimental thermo-fluid investigations of traction inverter cold plates have provided validated data to support model development and design optimization [16], [18]. Advanced heat spreading solutions for double-side-cooled modules have been evaluated to mitigate internal thermal gradients [17], while reliability-oriented studies have analyzed thermo-mechanical fatigue

The associate editor coordinating the review of this manuscript and approving it for publication was Gabriel Pinto (*Corresponding author: Leonardo Meinerz Abdalla*).

This work was supported by the Fundacao de Desenvolvimento da Pesquisa (FUNDEP), project number 27192*70.

Leonardo Meinerz Abdalla, P. H. Conrado, A. R. Rauber, L. R. Colpo, and F. Bruschi, are with the Instituto Hercilio Randon, Caxias do Sul, Brazil (e-mails: leonardo.meinerz@ihr.tec.br, paulo.conrado@ihr.tec.br, augusto.rauber@ihr.tec.br, leonardo.colpo@ihr.tec.br, and felipe.bruschi@terceiros.randon.com.br).

D. A. B. Zambra is with the Universidade Federal do Rio Grande do Sul (UFRGS), Tramandai, Brazil (e-mail: diorge.zambra@ufrgs.br).

mechanisms in SiC die attachments under thermal balancing strategies [19]. Furthermore, the impact of coolant transient conditions on SiC power modules has been examined, highlighting the importance of dynamic boundary condition modeling under rapid load and flow variations [20]. The Foster thermal model was developed to represent the heat transfer behavior of a liquid-cooled heatsink [21]. However, this approach describes only the overall thermal response of the system and does not allow the determination of intermediate temperatures.

Unlike previous Foster and Cauer studies, which have primarily focused on semiconductor-level thermal modeling or steady-state analyses, this work introduces a fully experimental methodology applied to an inverter heatsink. A distinctive aspect of the proposed approach is that the entire inverter housing functions as a heatsink, with the cooling channel machined directly into the aluminum casing. No dynamic thermal modeling studies addressing this specific configuration were identified in the reviewed literature. First, a controlled heating experiment was designed to overcome the limitations of segmented measurements, ensuring optimized sensor placement and simultaneous acquisition of all temperature data. Second, a refined Cauer-equivalent model was derived and validated, enabling accurate prediction of intermediate temperatures, which cannot be directly obtained from conventional Foster network structures. Third, the model was experimentally validated under severe operating conditions, establishing a direct correlation between heatsink thermal behavior and actual drive system performance, a perspective that remains largely unexplored in existing inverter thermal management research.

The developed model enables the assessment of whether thermal limitations may constrain the maximum power processed by the inverter, thereby supporting system-level design decisions. The scope of this study is restricted to the experimental characterization and dynamic modeling of the heatsink integrated into the analyzed inverter. Assumptions and limitations are discussed and summarized in the conclusion.

II. Methodology

The methodological approach adopted in this work integrates semiconductor loss estimation, synchronized temperature acquisition, and dynamic thermal modeling. First, conduction and switching losses of the IGBTs and diodes were calculated using electrical characteristics obtained from the FF225R12ME4_B11 datasheet, combined with the inverter modulation signals, load current profile, and computed switching instants. These losses defined the target power dissipation for the subsequent heating experiment.

Thermal measurements were collected simultaneously using four PT100 sensors mounted on the heat sink and two internal NTC sensors embedded within the IGBT modules. During the controlled heating test, the devices were biased in the linear region to replicate the average power dissipation expected during typical inverter operation, without applying full-load switching conditions. The recorded temperature responses enabled the identification of the heat sink thermal resistance and capacitance from both steady-state and transient behavior.

Finally, a complete Cauer-equivalent thermal network was constructed, incorporating device-level thermal impedances, interface resistance, and the identified heat sink parameters. The model was simulated under the same loss conditions as the experiment, allowing direct comparison between predicted and measured junction, case, and heat sink temperatures. This validation confirmed the accuracy of the model and provided a reliable basis for subsequent thermal analyses. By integrating experimental characterization with dynamic modeling, the proposed methodology enables the assessment of liquid-cooled heat sinks under realistic operating conditions.

III. Inverter

Fig. 1 shows a conventional three-phase, two-level inverter designed to power a permanent magnet synchronous motor (PMSM). The motor specifications are shown in Table I. This inverter uses three IGBT modules from Infineon (model FF225R12ME4_B11), which support 1200 V and 225 A, and employs the space vector modulation technique to control the semiconductors. The inverter uses field-oriented control to regulate the PMSM torque and speed.

IV. Semiconductor Power Losses Analysis

The estimation of power losses in semiconductors is achieved through the implementation of Algorithm 1. Initially, the input variables are defined as follows: the nominal frequency of the signal generated by the inverter (f), the frequency modulation index (m_f), the amplitude modulation index (m_a), the power factor (PF), the maximum line current (I_{max}), and the total number of

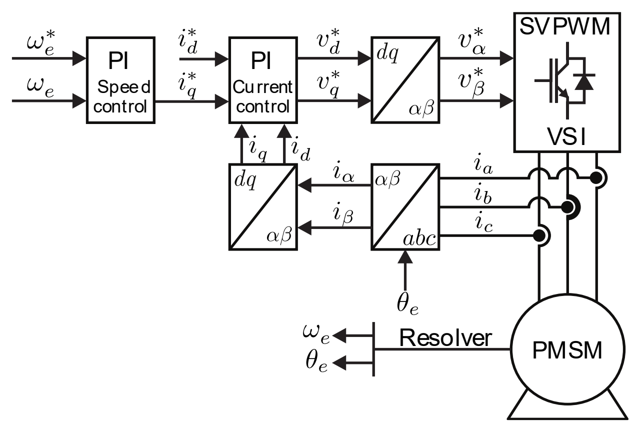

Fig. 1. Conventional PMSM drive system with a two-level three-phase inverter and field-oriented control (FOC).

TABLE I
RATED ELECTRICAL AND MECHANICAL SPECIFICATIONS OF THE PMSM

Specification	Value
RMS Phase-to-Neutral Voltage (V)	212
RMS Phase Current (A)	140
Frequencya (Hz)	270
Active Power (kW)	72
Torque (Nm)	214
Speed (RPM)	3250

simulation points (*cp*). Using these parameters, the reference period (*T*), the time vector (**t**), the phase angle of the load current (**θ**), and the load current itself ($\mathbf{I_L}$) are calculated.

The curves describing the voltage drop in IGBT conduction ($\mathbf{v_{ce}}$) and diode conduction ($\mathbf{v_f}$) were obtained from the FF225R12ME4_B11 module datasheet. The curves describing the energy dissipation in turn-on transitions ($\mathbf{E_{on}}$), turn-off transitions ($\mathbf{E_{off}}$), and reverse recovery of the diode ($\mathbf{E_{rec}}$) were also obtained from the datasheet. These parameters are contingent upon the line load current.

The command signals of the IGBT module of phase “a” ($\mathbf{Vcmd_1}$ and $\mathbf{Vcmd_2}$) are obtained by comparing the reference signal of phase “a” ($\mathbf{v_{refa}}$) with a triangular waveform ($\mathbf{v_{tri}}$). The conduction losses in IGBTs ($\mathbf{Pci_x}$), and diodes ($\mathbf{Pcd_x}$) are obtained from the product of $\mathbf{v_{ce}}$, $|\mathbf{I_L}|$ and $\mathbf{Vcmd_x}$, where *x* is either IGBT 1 or 2. The switching losses are obtained by identifying every turn-on, turn-off and reverse-recovery instant during one reference period. The turn-on ($\mathbf{Pon_x}$), turn-off ($\mathbf{Poff_x}$) and reverse-recovery losses ($\mathbf{Prec_x}$) are obtained through the average value of the sum of all lost energy. Finally, the total power losses (P_{tot}) are the sum of all the conduction and switching losses.

The utilization of Algorithm 1 was instrumental in simulating the inverter and estimating power losses in semiconductors. The simulation assumed a 20% motor overload, representing the worst-case operating condition. The total loss obtained was 2258.4 W, while the estimated power losses for a single IGBT and a diode were 258.3 W and 118.1 W, respectively. Fig. 2 illustrates the distribution of power losses in an IGBT and a diode. These loss values were utilized as a reference point for conducting the controlled heating test of the heat transfer system.

Algorithm 1 Power losses estimation

Inputs:
$f \leftarrow 270$
$m_f \leftarrow 37$
$m_a \leftarrow 1$
$\mathrm{PF} \leftarrow 0.7526$
$I_{max} \leftarrow 237.5$
$cp \leftarrow 300m_f$
Line current:
$T \leftarrow 1/f$
$\boldsymbol{\theta} \leftarrow 2\pi f\mathbf{t}$ **for** $\mathbf{t} \leftarrow 0{:}\frac{T}{cp-1}{:}T$
$\mathbf{I_L} \leftarrow m_a I_{max}\sin(\boldsymbol{\theta} - \mathrm{acos}(PF))$
Semiconductor model:
$\mathbf{v_{ce}} \leftarrow -0.00002\mathbf{I_L^2} + 0.012\mathbf{I_L} + 0.4698$
$\mathbf{v_f} \leftarrow -0.00001\mathbf{I_L^2} + 0.075\mathbf{I_L} + 0.5424$
$\mathbf{E_{on}} \leftarrow (0.0000004\mathbf{I_L^3} + 0.0002\mathbf{I_L^2} + 0.0726\mathbf{I_L} + 1.365)0.001$
$\mathbf{E_{off}} \leftarrow (0.00004\mathbf{I_L^2} + 0.128\mathbf{I_L} + 2.497)0.001$
$\mathbf{E_{rec}} \leftarrow (0.0000003\mathbf{I_L^3} - 0.0004\mathbf{I_L^2} + 0.1555\mathbf{I_L} + 5.0536)0.001$
Command signals:
$\mathbf{v_{refa}} \leftarrow m_a\sin(2\pi f\mathbf{t})$
$\mathbf{t_{ri}} \leftarrow sawtooth(2\pi f m_f\mathbf{t}, 0.5)$
$\mathbf{Vcmd_1} \leftarrow 1$ **if** $\mathbf{v_{refa}} \geq \mathbf{t_{ri}}$ **else** $\mathbf{Vcmd_1} \leftarrow 0$
$\mathbf{Vcmd_2} \leftarrow 0$ **if** $\mathbf{Vcmd_1} = 1$ **else** $\mathbf{Vcmd_2} \leftarrow 1$
Power losses:
$\mathbf{Pci}_x = \frac{1}{T}\mathbf{v_{ce}}|\mathbf{I_L}|\mathbf{Vcmd_x}$ **for** $x = 1{:}2$
$\mathbf{Pcd}_x = \frac{1}{T}\mathbf{v_f}|\mathbf{I_L}|\mathbf{Vcmd_x}$ **for** $x = 1{:}2$
$\mathbf{E_{onTx}} \leftarrow \mathbf{E}_{on}$ **if** $\mathbf{Vcmd_x}(t) = 0\ \&\ \mathbf{Vcmd_x}(t+1) = 1\ \&\ \mathbf{I}_L(t) \geq 0$ **else** $\mathbf{E_{onT}} \leftarrow 0$
$\mathbf{E_{offTx}} \leftarrow \mathbf{E}_{off}$ **if** $\mathbf{Vcmd_x}(t) = 1\ \&\ \mathbf{Vcmd_x}(t+1) = 0\ \&\ \mathbf{I}_L(t) \geq 0$ **else** $\mathbf{E_{offT}} \leftarrow 0$
$\mathbf{E_{recTx}} \leftarrow \mathbf{E}_{rec}$ **if** $\mathbf{Vcmd_x}(t) = 1\ \&\ \mathbf{Vcmd_x}(t+1) = 0\ \&\ \mathbf{I}_L(t) < 0$ **else** $\mathbf{E_{recT}} \leftarrow 0$
$\mathbf{Pon}_x = \frac{1}{T}\sum\mathbf{E_{onTx}}$ **for** $x = 1{:}2$
$\mathbf{Poff}_x = \frac{1}{T}\sum\mathbf{E_{offTx}}$ **for** $x = 1{:}2$
$\mathbf{Prec}_x = \frac{1}{T}\sum\mathbf{E_{recTx}}$ **for** $x = 1{:}2$
$\mathbf{P_{ix}} = Pci_x + Pon_x + Poff_x$ **for** $x = 1{:}2$
$\mathbf{P_{dx}} = Pcd_x + Prec_x$ **for** $x = 1{:}2$
$P_{tot} = 3(P_{i1} + P_{d1} + P_{i2} + P_{d2})$

V. Heat Transfer System

A. Liquid Cooling System

The drive systems of electric and hybrid vehicles are cooled by electromechanical, hydraulic, and mechanical components. These components transfer heat from the cooling fluid to the environment, ensure the fluid moves at the correct pressure and flow rate, and store and filter the fluid to prevent contamination. A hydraulic pump, heat exchanger, reservoir, and filter are necessary for the cooling system to function properly. Fig. 3 illustrates the connection between the cooling system elements and the inverter and permanent magnet synchronous motor (PMSM).

The implemented cooling system consists of the following:

a) A hydraulic gear pump suitable for operating with oil. It has a flow rate of 30 L/min and a pressure of 1 bar.

b) An expansion tank that is pressurized and capable of storing 1.5 L at a pressure of 1 bar.

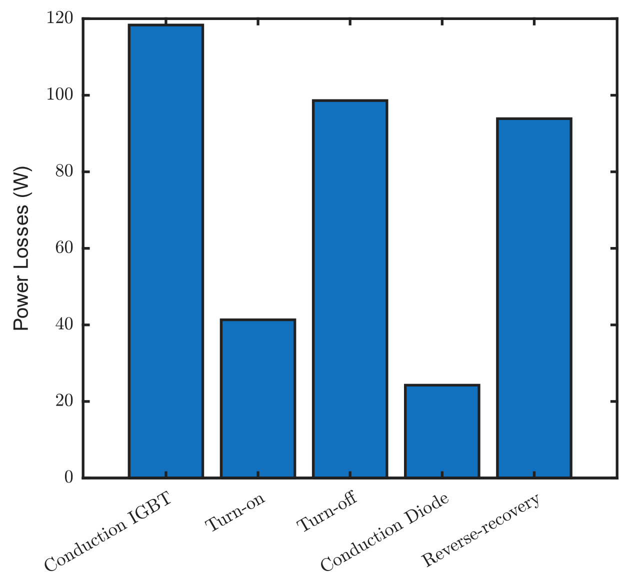

Fig. 2. Power losses distribution for one IGBT and one diode.

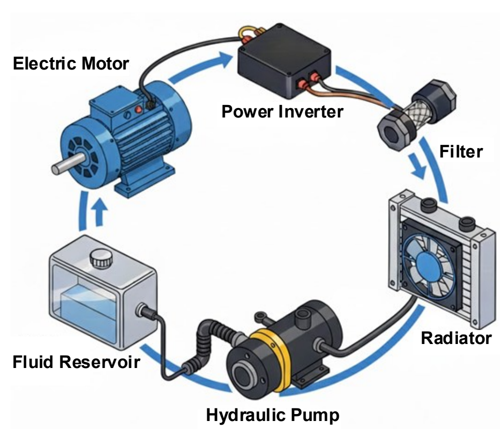

Fig. 3. Liquid cooling system architecture showing the cooling circuit and its connection to the inverter and PMSM.

c) A radiator with a 385 mm diameter fan, an airflow rate of 3,690 m³/h, and an IP68 degree of protection.

d) An oil return filter installed in the line with filter elements of 30, 80, and 150 microns.

e) Dielectric oil with viscosities of 9.79 cSt at 40 °C and 2.44 cSt at 100 °C.

f) A coil machined into the inverter housing to cool the IGBT modules. Fig. 4 shows the dielectric oil circulation channel for cooling the IGBT modules.

The dynamic model of the cooling system represents all elements as a single resistance and a single capacitance.

B. Controlled Heating Experiment

The controlled heating test biases the IGBT in the linear region to match the average power dissipation of real inverter operation. The thermal network was modeled dynamically, with the IGBT junction-to-case impedance as a Cauer model, the thermal interface material as a series resistance, and the heatsink as an RC network extracted from the continuous heating test, terminating at ambient temperature. This configuration captures both transient junction and case temperatures as well as the quasi-steady-state response of the heatsink. Limitations include filtering of high-frequency switching losses and the assumption of unidirectional heat flow, neglecting lateral spreading. As a result, while average temperatures and slow transients are accurately predicted, instantaneous spatial distributions, rapid 10 kHz switching oscillations, and local hotspots are not fully reproduced.

The controlled heat sink heating experiment enables the extraction of the dynamic model of the cooling system without operating the inverter at its nominal power. Due to the current limitation of the laboratory power supply, the test was conducted using only two of the inverter IGBTs. This adaptation does not compromise the results, since the time required for the system to reach thermal steady state remains unchanged, as the thermal dynamics are primarily governed by the thermal properties of the assembly (thermal capacitance and thermal resistance), rather than by the number of active devices. If the dissipated power is increased, the steady-state temperature will rise accordingly, however, the heating dynamics remain unaffected. Furthermore, because the temperature variation is proportional to the dissipated power, the observed thermal behavior remains representative of the complete system.

The assembly of the system began with the installation of two IGBT modules in the inverter cabinet, highlighted in red on Fig. 4. To enable simultaneous measurements, four PT100 temperature sensors were installed on the heat sink. Two of these sensors were positioned close to the modules subjected to controlled heating, while the other two measurements corresponded to the internal NTC sensors of each module, as illustrated in Fig. 4. A data acquisition system was responsible for simultaneously recording the six temperatures, four from the PT100 sensors and two from the NTC sensors.

After the assembly of the system, the power supplies were configured. For this adjustment, the collector current curve (I_C) as a function of the gate-emitter voltage (V_{GE}) was utilized as a reference. The value of V_{GE} = 7.4 V was defined to ensure the operation of the IGBT in the linear region. This voltage level enables the dissipation of the power estimated from the loss analysis, corresponding to 376.4 W per IGBT, without the necessity of 168 Arms conduction and 10 kHz switching. In these conditions, the collector-emitter voltage (V_{CE}) was measured to be 14.97 V with a current of 25.95 A in module one and 15.11 V with a current of 26.68 A in module two. These measurements yielded an average dissipation of approximately 395 W per module, as depicted in Fig. 5.

After assembling the system, configuring the power supplies, and installing the data acquisition system, a controlled heating test was performed. Initially, the cooling system was activated, and then the V_{GE} and V_{CE} voltages were applied simultaneously. Temperature acquisition began with the application of the V_{CE} voltage. To assess the reliability of the measurements obtained by the PT100 and NTC sensors, a thermal imaging camera was used to measure the temperature at the focal point. Fig. 6 shows the temperatures recorded by the sensors over time. The data were not filtered or subjected to any treatment, which explains the oscillations observed in the NTC sensor signals, possibly due to noise.

To improve the scientific rigor and reliability of the experimental validation, a measurement uncertainty analysis was performed. The heatsink temperature was measured using a Class A PT100 sensor with an accuracy of ± (0.15 + 0.002|T|) °C according to IEC 60751 [22]. The intrinsic NTC sensor integrated into the IGBT module has a resistance tolerance of ±5% at 100°C, corresponding to an estimated temperature uncertainty of approximately ±1.5°C within the operating temperature range [23]. Surface temperature distributions were obtained using a FLIR E4 thermal camera with a specified accuracy of ±2°C or ±2% of the reading [24]. The PT100 and

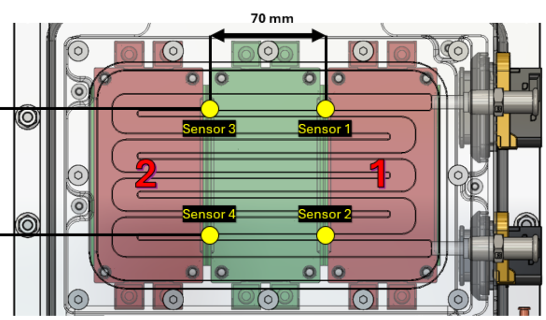

Fig. 4. Heat sink assembly showing the coolant circulation channel, IGBT modules, and temperature sensor locations.

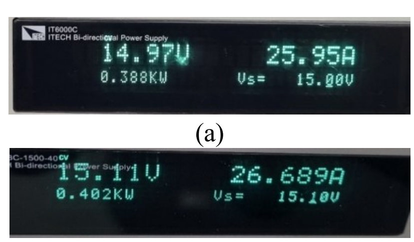

(a)

(b)

Fig. 5. Power dissipation in semiconductors: a) IGBT 1; b) IGBT 2.

NTC measurements were used for quantitative validation of the corresponding thermal nodes of the proposed model, while the thermal camera was employed to verify the predicted temperature distribution and hot-spot locations. For the heatsink temperature validation, the comparison between the model and experimental measurements resulted in a mean absolute error of approximately 0.4°C and a maximum deviation of 1.46°C, demonstrating good agreement between the proposed thermal model and the experimental data.

Fig. 7a shows the temperature measured in the IGBT 1 case, which had the gate drive installed in the module, while Fig. 7b shows the temperature of the IGBT 2 encapsulation, without a gate drive. There is a difference of 20 °C between the measurements, attributed to the distance between the gate drive and the module encapsulation. Therefore, the measurement obtained from the module without the gate drive was selected as the reference value, presenting a temperature of 63.2 °C, while the acquisition system recorded 59.49 °C and 58.42 °C, indicating good agreement between both measurement methods.

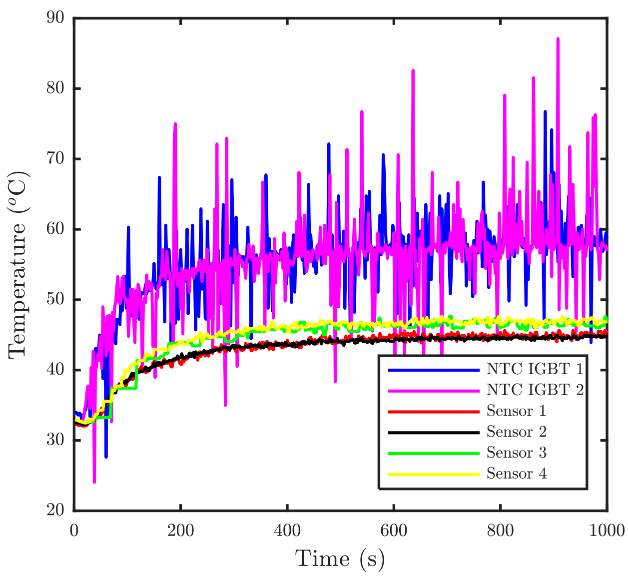

Fig. 6. Simultaneous temperature measurements.

Fig. 7(c) shows a temperature of 45.2 °C and Fig. 7(d) shows a temperature of 47.8 °C, both obtained using the thermal imaging camera. At these same positions, sensors 1 and 2 recorded temperatures of 45.21 °C and 44.6 °C, respectively. Similarly, Fig. 7(e) shows a temperature of 45.6 °C and Fig. 7(f) shows a temperature of 48.0 °C, also measured with the thermal imaging camera. For these points, sensors 3 and 4 indicated temperatures of 46.64 °C and 47.22 °C, respectively. Together, these measurements confirm the reliability of the temperature measurements obtained from the data acquisition system.

C. Determining the Dynamic Model

After carrying out the controlled heating test, it is possible to obtain a dynamic model of the heat sink. The procedure begins by determining the total temperature variation (ΔT), given by

$$\Delta T = T_{HS} - T_a, \tag{1}$$

where, T_a is the ambient temperature, measured before the heating process begins, and T_{HS} is the final heat sink temperature. The thermal resistance of the heat sink (R_{TH}) is then calculated as

$$R_{TH} = \frac{\Delta T}{P_{totx}}, \tag{2}$$

where P_{totx} is the power dissipated by the IGBT during the heating process. Finally, the thermal capacitance (C_{TH}) is obtained from

$$C_{TH} = \frac{\tau}{R_{TH}}, \tag{3}$$

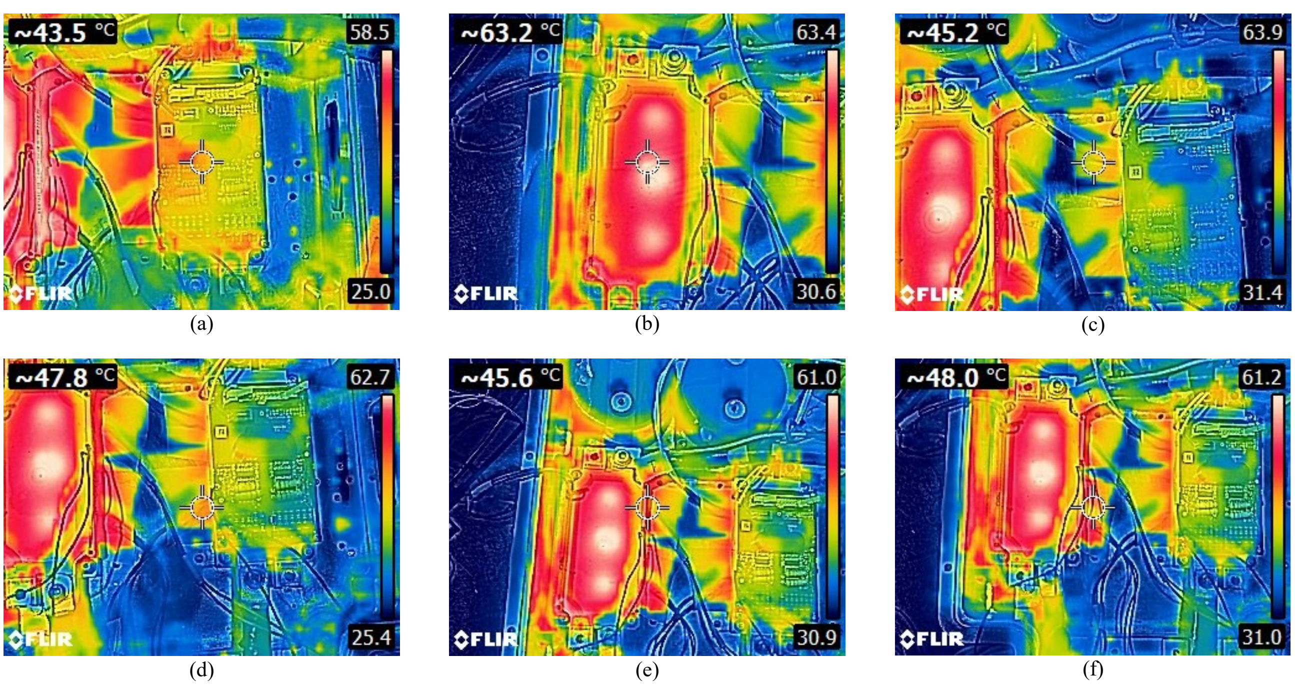

Fig. 7. Temperatures: a) case IGBT 1 with gate drive; b) case IGBT 2 without IGBT2; c) sensor 1; d) sensor 2; e) sensor 3; f) sensor 4.

where τ is the thermal time constant of the system, corresponding to the time required for the heat sink temperature to reach approximately 63.2% of its total variation following a step change in the dissipated power.

The average temperature of sensors 1, 2, 3 and 4 (Fig. 6) was used to obtain a dynamic model of the heat sink. The extracted data are as follows: ambient temperature of 32.68 °C, final heat sink temperature of 45.92 °C, time required to reach a temperature of 45.92 °C of 972 seconds, and dissipated power of 790 W. These values result in a thermal resistance of 16.75 m°C/W and a thermal capacitance of 6444.3 J/°C.

The dynamic model (Fig. 8) was simulated, and its response was plotted alongside the reference curve (Fig. 9) for validation purposes. A strong agreement between the reference curve and the simulated results can be observed. To provide a quantitative assessment of the model accuracy, the Root Mean Square Error (RMSE) was calculated, resulting in a value of 0.84 °C. This low RMSE confirms the high predictive accuracy of the proposed thermal model.

VI. Validation of the Heat Transfer System

The thermal behavior of semiconductors can be described using various equivalent circuits. In Foster's thermal model, commonly provided by semiconductor manufacturers and used in analytical calculations, the coefficients are easily extracted from measured heating/cooling curves. However, its intermediate nodes lack physical significance, providing access only to the junction temperature. Conversely, the Cauer model represents the physical concept of individual layers heating up sequentially. By directly assigning RC elements to components such as the chip, solder, and substrate, the Cauer network's intermediate nodes possess physical significance, allowing access to the temperatures of internal interfaces [25].

The heat transfer system was evaluated using the Cauer equivalent circuit, obtained from a mathematical transformation of the Foster model. Appendix I presents the thermal resistances and capacitances of the IGBTs and diodes associated with the Foster model, as well as the parameters of the Cauer equivalent circuit. The complete thermal circuit is illustrated in Fig. 10 and includes the dynamic model of a single IGBT and a diode. The power losses of the second IGBT and the second diode belonging to the same module are considered through the current sources P_{i2} and P_{d2}. The losses of module 1 are injected at the case node (T_c). In turn, the losses of the other semiconductors are represented by equivalent current sources, namely $P_{i3}+P_{i4}+P_{i5}+P_{i6}$ for IGBTs and $P_{d3}+P_{d4}+P_{d5}+P_{d6}$ for the diodes. The total sum of losses is injected into the heat sink node (T_{HS}) and propagated through its dynamic model.

Fig. 11 shows the dynamic temperature response when two

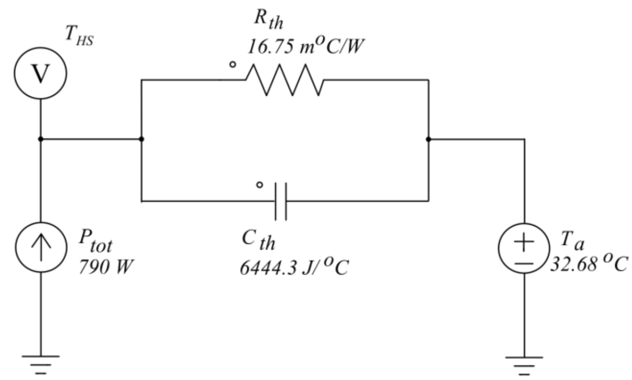

Fig. 8. Simulation of the dynamical model.

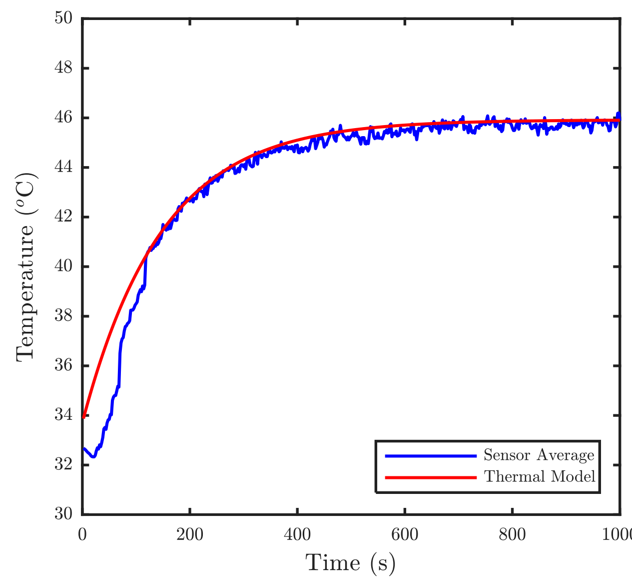

Fig. 9. Comparison of the dynamic model results and the reference curve.

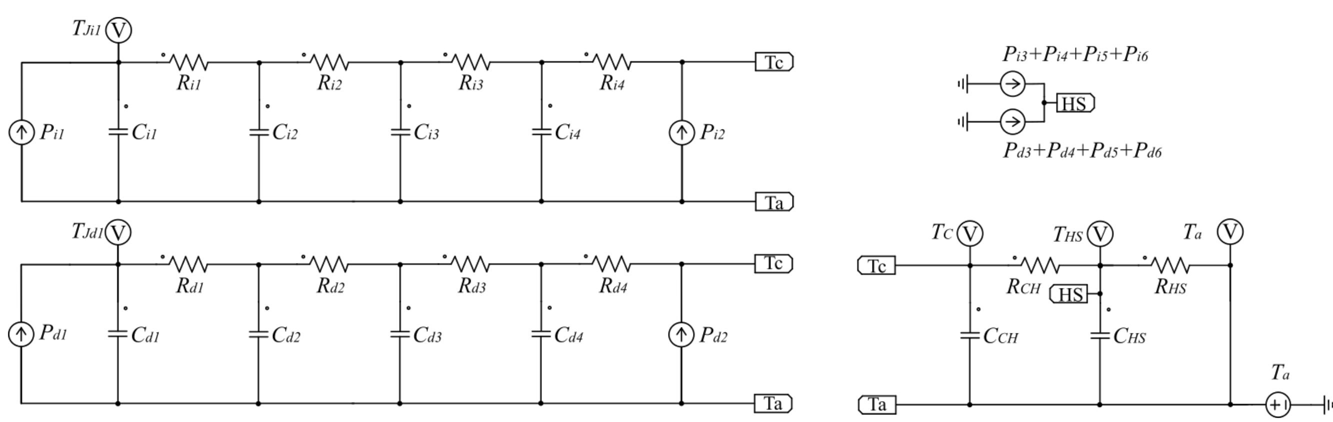

Fig. 10. Cauer thermal model.

IGBTs are subjected to losses of 395 W, a condition equivalent to that of the controlled heating test. After reaching steady state, the junction temperatures of the IGBT and diode reach 92.67 °C and 80.74 °C, respectively. The heat sink temperature (T_{HS}) stabilizes at 45.13 °C, while the module encapsulation temperature (T_C) reaches 56.72 °C.

Fig. 12 presents the dynamic temperature response of the complete inverter, comprising six IGBTs and six diodes. In this simulation, the junction temperatures of the IGBTs and diodes reach steady-state values of 130.47 °C and 118.53 °C, respectively. Both values remain below the critical limit of 150 °C, ensuring an adequate thermal margin under the evaluated operating conditions.

From a practical standpoint, maintaining junction temperatures below the maximum rated limit contributes directly to improved device reliability. A sufficient thermal margin reduces thermo-mechanical stress caused by temperature swings, thereby mitigating thermal-cycling effects on bond wires and solder layers, mechanisms commonly associated with wear-out failures in power semiconductor modules. Consequently, the predicted operating temperatures indicate a lower risk of accelerated aging and support an extended service lifetime of the inverter under real operating conditions.

Additionally, the results show that the heat sink and encapsulation temperatures stabilize at 94.52 °C and 71.01 °C, respectively, confirming adequate heat dissipation and supporting stable long-term operation of the system.

VII. EXPERIMENTAL RESULTS

Fig. 13 shows a dynamometer bench developed to conduct

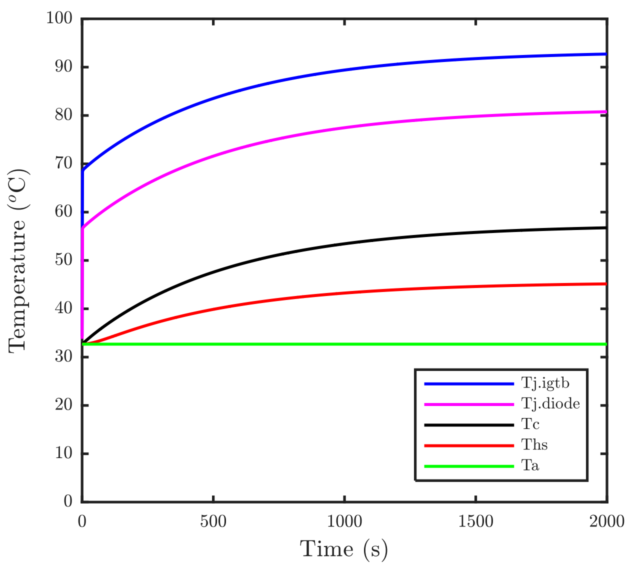

Fig. 11. Transient thermal response of the system for 2 IGBTs.

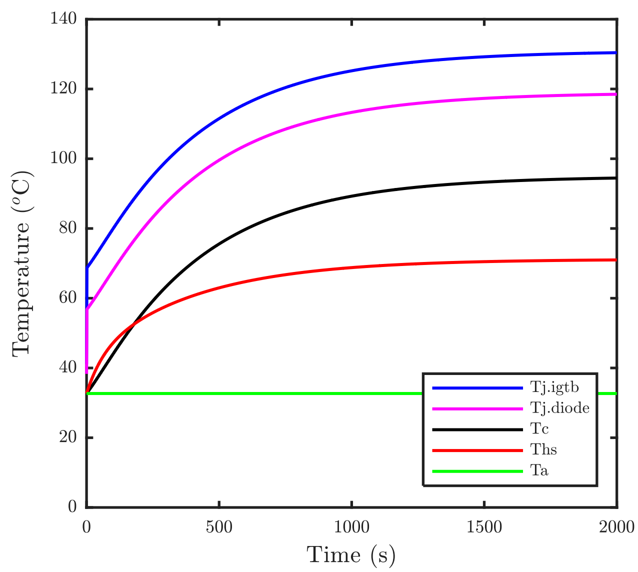

Fig. 12. Transient thermal response of the system for 6 IGBTs.

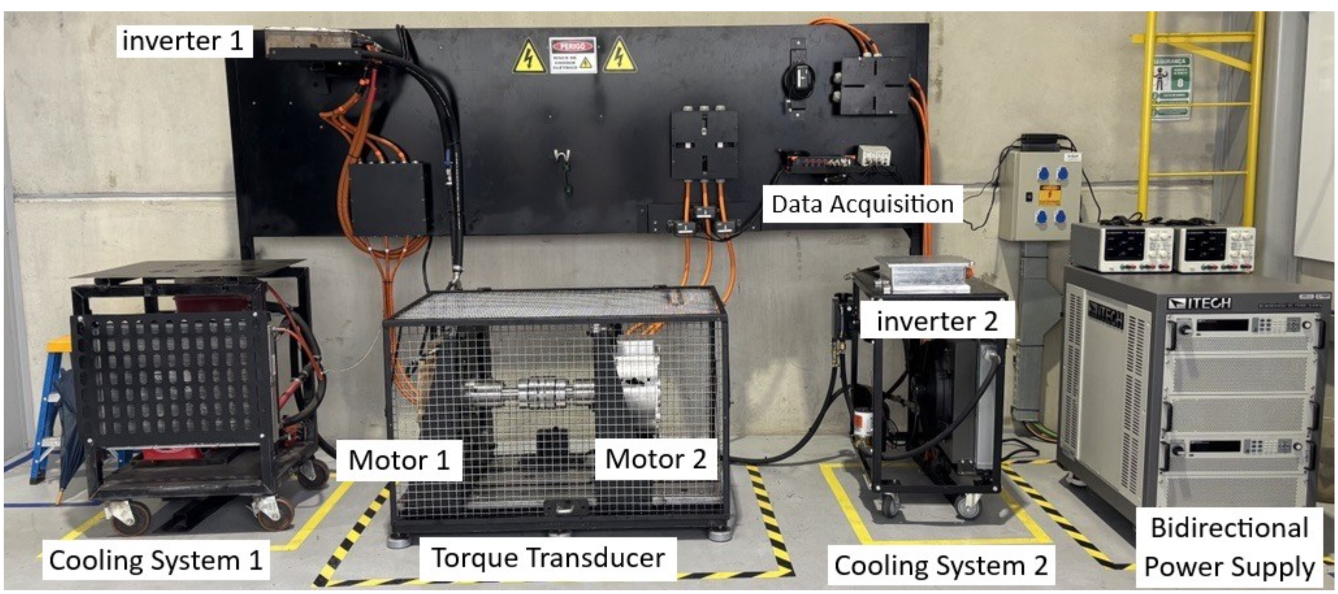

Fig. 13. Dynamometer test bench used for the experimental validation of the inverter loss and temperature estimation.

tests intended to validate the estimation of losses and temperatures of the IGBT modules in the inverter cooled by the thermal management system that was modeled in this study. The test bench consists of two sets, each comprising a cooling system, a permanent magnet synchronous motor (PMSM), and an inverter. One of the sets functions under speed control, operating as a motor, while the other operates under torque control, functioning as a generator. Both inverters are supplied by a bidirectional power supply. The inverter output voltages and currents were measured using an HBM Generation 3i power analyzer with eDrive Testing software. The waveforms of the three-phase voltages and currents of the inverter are illustrated in Fig. 14. The temperatures of the three IGBT modules were obtained using TSMaster software through the inverter's CAN communication functionality.

Fig. 15 presents the numerical values of the monitored variables during the test. The variables ΣI and ΣU represent the average values of the three RMS output currents and voltages of the inverter. The inverter's active power output is denoted by P. The power factor is represented by λ, T corresponds to the motor torque, while Idc refers to the supply current of the monitored inverter.

The numerical results of the variables of interest are summarized in Table II. The inverter input power was 65.86 kW, and the output power was 63.52 kW, resulting in power losses of 2.34 kW. Under these conditions, the temperatures of the IGBT modules were 79 °C, 80 °C, and 74 °C. The estimated power losses were 194.83 W for each IGBT and 101.80 W for each diode. This resulted in an encapsulation temperature of 80.48 °C.

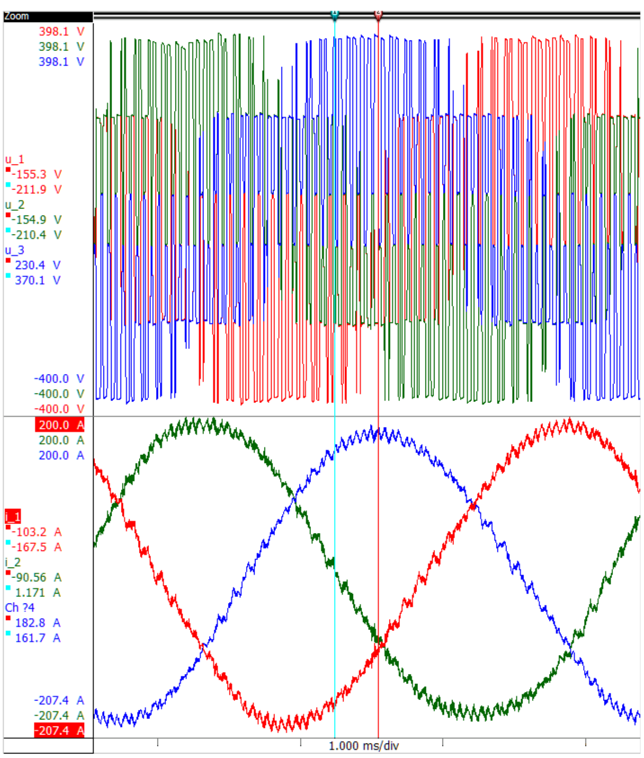

Fig. 14. Measured three-phase output voltage and current waveforms of the inverter during experimental testing.

VIII. Conclusion

This paper presents the thermal characterization and modeling of a liquid-cooled heat sink applied to a three-phase inverter for use in electric and hybrid vehicles. Controlled heating tests showed that the heat sink reached a steady-state temperature of 45.92 °C after 972 seconds with a dissipated power of 790 W. From these experimental data, the equivalent RC thermal model parameters were identified as R_{TH} = 16.75 m°C/W and C_{TH} = 6444.3 J/°C.

The corresponding Cauer thermal network incorporating the heat sink and semiconductor devices was simulated using estimated power losses. This resulted in maximum junction temperatures of 130.47 °C for the IGBTs and 118.53 °C for the diodes, remaining well within the 150 °C safety limit. Experimental validation under inverter operating conditions

TABLE II
Experimental Measurements and Operating Conditions Used for Model Validation

Parameter	Value
Battery bank voltage (Vdc)	587.00
Battery bank current (Adc)	112.20
Power supplied by battery bank (kW)	65.86
RMS phase voltage (Vrms)	218.40
RMS phase current (Arms)	128.80
Active power (kW)	63.52
Inverter losses (kW)	2.34
Torque (Nm)	178.00
Speed (RPM)	3200
Case temperature of the IGBT module of phase A (°C)	79
Case temperature of the IGBT module of phase B (°C)	80
Case temperature of the IGBT module of phase C (°C)	74

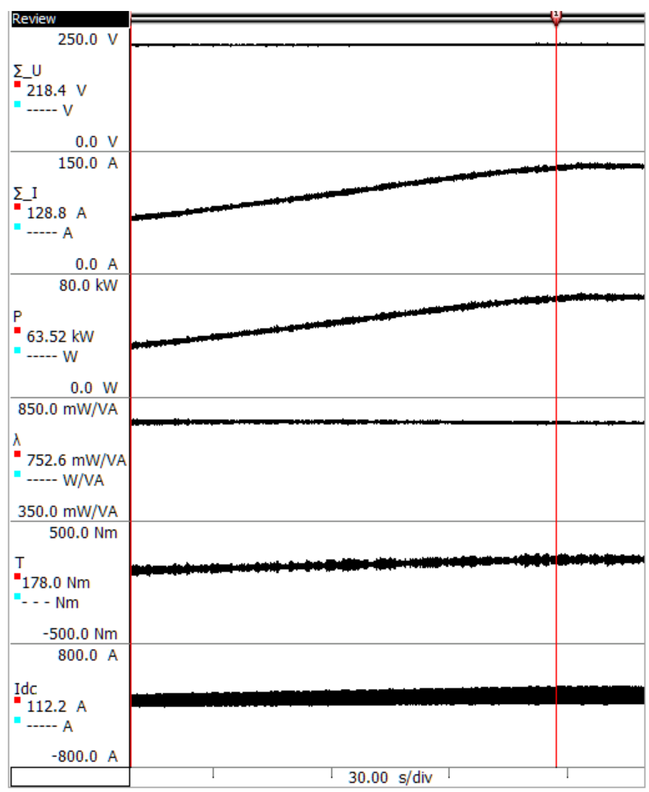

Fig. 15. Measured inverter input and output electrical and mechanical variables during the experimental test.

(65.86 kW input power) showed total power losses of 2.34 kW and an average IGBT package temperature of 77 °C. This closely matches the model's prediction of 80.48 °C, confirming the accuracy and applicability of the proposed thermal model for inverter thermal analysis.

The implications of this work allow for more accurate thermal management sizing, contributing to the reduction of drivetrain volume and mass without compromising reliability. Furthermore, the proposed model aids in defining safe operating limits and optimizing cooling system control strategies through reliable junction temperature prediction. Future work should focus on validating the model under dynamic drive cycles and varying operating conditions to assess transient thermal behavior in real-world driving scenarios. Additionally, further research is recommended to investigate the impact of different coolant flow rates and to extend this modeling approach to wide-bandgap (WBG) devices, such as silicon carbide (SiC) MOSFETs, which present higher power density challenges.

Appendix - Semiconductors Thermal Model

The transient thermal impedances of the Foster thermal model are specified in Table III. The datasheet for the FF225R12ME4_B11 module [23] provides the thermal resistances (R_f) and time constants (τ_f). The thermal capacitances (C_f) are obtained from R_f and τ_f using (3). The subscript "i" is used to denote the IGBT, while "d" indicates the diode.

The Foster model does not assign explicit physical meaning to its internal nodes. However, it is widely used in technical datasheets because its coefficients can be extracted directly from the measured cooling curve of the module [25]. In contrast, the Cauer thermal model reflects the actual physical structure of the semiconductor device, with thermal capacitances and intermediate thermal resistances representing individual material layers. The methodology for converting a Foster representation into an equivalent Cauer network is presented in [26]. The resulting Cauer parameters are summarized in Table IV.

TABLE III
FOSTER THERMAL NETWORK PARAMETERS USED FOR THE TRANSIENT THERMAL MODEL.

Parameter	Z1	Z2	Z3	Z4
R_{fi} (K/W)	0.0084	0.0462	0.0448	0.0406
τ_{fi} (s)	0.01	0.02	0.05	0.1
C_{fi} (J/K)	1.1904	0.4329	1.1161	2.4631
R_{fd} (K/W)	0.0114	0.0627	0.0608	0.0551
τ_{fd} (s)	0.01	0.02	0.05	0.1
C_{fd} (J/K)	0.8772	0.3190	0.8224	1.8149

TABLE IV
CAUER THERMAL NETWORK PARAMETERS OBTAINED FROM THE FOSTER MODEL.

Parameter	Z1	Z2	Z3	Z4
R_i (K/W)	0.0895	0.0288	0.0182	0.0035
C_i (J/K)	0.2246	0.6960	1.8640	21.1135
R_d (K/W)	0.1215	0.0391	0.0248	0.0047
C_d (J/K)	0.1655	0.5128	1.3736	15.5591

References

[1] S. M. S. H. Rafin, R. Islam and O. A. Mohammed, "Overview of Power Electronic Converters in Electric Vehicle Applications," *2023 Fourth International Symposium on 3D Power Electronics Integration and Manufacturing (3D-PEIM)*, Miami, FL, USA, 2023, pp. 1-7. DOI: 10.1109/3D-PEIM55914.2023.10052532

[2] C. Sachs e M. Neuburger, "A Data-Based Review of Battery Electric Vehicle and Traction Inverter Trends," na *IECON 2025 - 51st Annual Conference of the IEEE Industrial Electronics Society*, 2025. DOI: 10.48550/arXiv.2508.14224

[3] F. Aguilera, P. M. de la Barrera and C. H. De Angelo, “Selection of Induction Machine Models for Efficiency Evaluation in Electric Vehicles,” IEEE Latin America Transactions, vol. 11, no. 1, pp. 334–340, Feb. 2013. DOI: 10.1109/TLA.2013.6502826

[4] P. H. A. S. e. Silva, L. A. B. Viera, R. Camponogara, H. Pinheiro and R. P. Vieira, "Analysis of the Impact of Semiconductor Losses in High-Density Power Inverters," IEEE 8th Southern Power Electronics Conference and 17th Brazilian Power Electronics Conference, 2023, pp. 1-6. DOI: 10.1109/SPEC59248.2023.10355877

[5] T. E. Salem, S. B. Bayne, D. Porschet and Y. Chen, "Thermal performance of water-cooled heat sinks," Twentieth Annual IEEE Applied Power Electronics Conference and Exposition, 2005, pp. 129-133, v.1. DOI: 10.1109/APEC.2005.1452902

[6] P. H. A. S. e. Silva, E. C. Silva, L. R. Rocha, L. A. B. Viera and R. P. Vieira, "Study and Evaluation of Liquid Cooling Heat Sinks for High Power Density Inverters," IEEE 8th Southern Power Electronics Conference and 17th Brazilian Power Electronics Conference, 2023, pp. 1-6. DOI: 10.1109/SPEC59248.2023.10355878

[7] R. Aqeel, M. Aashquin, A. Raza, H. Ali, and S. Ahmed, “Effect of Heat Sink Configuration on the Performance of Thermoelectric Refrigeration,” in Proc. IEEE Latin America Electron Devices Conf. (LAEDC), Apr. 2021, pp. 1-4. DOI: 10.1109/LAEDC51812.2021.9437978.

[8] B. Li, X. Yang, K. Wang, H. Zhu, L. Wang and W. Chen, A compact double-sided cooling 650V/30A GaN power module with low parasitic parameters, IEEE Transactions on Power Electronics, vol. 37, no. 1, pp. 426-439, 2022. DOI: 10.1109/TPEL.2021.3092367

[9] R. Šprlák, D. Kalvar, J. Opluštil and P. Chlebiš, "Design of experimental liquid heat sink for high power electronic," 2014 14th International Conference on Environment and Electrical Engineering, Poland, 2014, pp. 392-396. DOI: 10.1109/EEEIC.2014.6835873

[10] D. DeVoto and P. McCluskey, "Reliability modeling of a single phase liquid cooling system for power electronics applications," 2010 12th IEEE Intersociety Conference on Thermal and Thermomechanical Phenomena in Electronic Systems, Las Vegas, USA, 2010, pp. 1-5. DOI: 10.1109/ITHERM.2010.5501363

[11] P. H. A. S. e Silva, E. C. da Silva, L. R. Rocha, P. R. Eckert and R. P. Vieira, "Analysis and Modeling of a Liquid Cooled Heat Sink for EV Traction Inverter Systems," 2022 IEEE Transportation Electrification Conference & Expo (ITEC), 2022, pp. 825-830. DOI: 10.1109/ITEC53557.2022.9813808

[12] G. R. Bruzinga, A. J. Sguarezi Filho and A. Pelizari, “Analysis and Design of 3 kW Axial Flux Permanent Magnet Synchronous Motor for Electric Car,” IEEE Latin America Transactions, vol. 20, no. 5, pp. 855–863, May 2022. DOI: 10.1109/TLA.2022.9693571

[13] A. Chatterjee, M. Anwar, R. Shivshankar, V. Bhaskar, V. Nukala and N. Bajoria, "Thermal Modelling of EV Inverters: Physical Models to Thermal Networks for Advanced Power Modules," 2025 IEEE Energy Conversion Conference Congress and Exposition (ECCE), Philadelphia, PA, USA, 2025, pp. 1-6. DOI: 10.1109/ECCE58356.2025.11259658.

[14] X. Chen, X. Xu, M. Li, Y. Li and H. Ling, "Prediction of SiC MOSFET Power Modules Junction Temperature for Electric Vehicle Based on Electro-Thermal Coupled Model," 2024 IEEE 22nd International Conference on Industrial Informatics (INDIN), Beijing, China, 2024, pp. 1-6. DOI: 10.1109/INDIN58382.2024.10774495.

[15] A. Kempitiya and W. Chou, "Electro-thermal analysis for automotive high power MOSFETs," 2017 33rd Thermal Measurement, Modeling & Management Symposium (SEMI-THERM), San Jose, CA, USA, 2017, pp. 302-305. DOI: 10.1109/SEMI-THERM.2017.7896945.

[16] V. Ravindra, P. Elango and P. Prasad, "Experimental Investigation of Flow and Thermal Characteristics of Traction Inverter cold plate," 2025 IEEE Energy Conversion Congress & Exposition Asia (ECCE-Asia), Bengaluru, India, 2025, pp. 1-6. DOI: 10.1109/ECCE-Asia63110.2025.11112026.

[17] G. Moreno et al., "Evaluation of Heat Spreading Technologies Within Double-Side-Cooled Power Modules," 2025 Fifth International Symposium on 3D Power Electronics Integration and Manufacturing (3D-PEIM), Denver, CO, USA, 2025, pp. 1-8. DOI: 10.1109/3D-PEIM64703.2025.11180271.

[18] V. Ravindra, P. Elango and P. Prasad, "Experimental Investigation of Flow and Thermal Characteristics of Traction Inverter cold plate," 2025 IEEE Energy Conversion Congress & Exposition Asia (ECCE-Asia), Bengaluru, India, 2025, pp. 1-6. DOI: 10.1109/ECCE-Asia63110.2025.11112026.

[19] L. Zhou et al., "Reliability Study of Die Attachments in SiC Power Modules with Thermal Balancing Control," 2025 IEEE/AIAA Transportation Electrification Conference and Electric Aircraft Technologies Symposium (ITEC+EATS), Anaheim, CA, USA, 2025, pp. 1-5. DOI: 10.1109/ITEC63604.2025.11097929.

[20] C. Zhang and R. Negri, "Analysis of Coolant Transients Impact on SiC Power Module in Traction Inverter," PCIM Conference 2025; International Exhibition and Conference for Power Electronics, Intelligent Motion, Renewable Energy and Energy Management, Nürnberg, Germany, 2025, pp. 2790-2795. DOI: 10.30420/566541374.

[21] D. A. B. Zambra, L. M. Abdalla, P. H. Conrado, A. R. Rauber, and L. R. Colpo, "Evaluating a Liquid Cooled Heatsink for Drive Systems used in Hybrid Electric Vehicles," in *INDUSCON 2025 - IEEE International Conference on Industry Applications*, 2025, pp. 1–6. DOI: 10.1109/INDUSCON66435.2025.11241641.

[22] Siemens AG, "PT100 Resistance Thermometer, Technical Data," Document No. CA1N1714E, Nov. 1998. Available: https://sid.siemens.com/v/u/20052

[23] *Datasheet:* EconoDUAL™3 module with Trench/Fieldstop IGBT4 and emitter controlled HE diode and PressFIT / NTC - FF225R12ME4_B11, Infineon Technologies AG, Munich, DE, 2024, p. 14. Available: https://www.infineon.com/

[24] FLIR Systems, "FLIR E4 Infrared Camera Datasheet," Publ. No. 63901-0101, Dec. 2014. Available: https://www.flir.com/pt-br/products/e4/

[25] *Technical Information*: Transient thermal measurements and thermal equivalent circuit models – AN2015-10, Infineon Technologies AG, Munich, DE, p. 11. Available: https://www.infineon.com/

[26] K. Murthy and R. Bedford, "Transformation between Foster and Cauer equivalent networks," in IEEE Transactions on Circuits and Systems, vol. 25, no. 4, pp. 238-239, April 1978. DOI: 10.1109/TCS.1978.1084459.

Leonardo Meinerz Abdalla received his B.S degree in Control and Automation Engineering from the Federal University of Santa Maria (UFSM), Santa Maria, RS, Brazil, in 2023, and completed a specialization in Automotive Engineering at Anhanguera, Brazil, in 2025. He is currently pursuing a postgraduate degree in Occupational Safety Engineering, expected to finish in September 2026. His main field of study is electrical and automotive engineering. He works as a Science and Technology Analyst at Instituto Hercilio Randon, located in Farroupilha, RS, Brazil. His experience includes volunteer participation in SAE competitions and activities related to research, development, and normative testing. His current and previous research interests include power electronics, electric machines, traction inverters, vehicle electrification systems, normative tests and test benches, patent search and prospecting, smart grids, fuel cells and hydrogen, as well as solar energy systems. He also aims to contribute to initiatives focused on technological innovation and the development of solutions for mobility and energy.

Paulo Henrique Conrado received his B.S. degree in electrical engineering from the Universidade de Caxias do Sul (UCS), Caxias do Sul, Brazil, in 2017, and the postgraduate degree in project management from the Fundacao Getulio Vargas (FGV), Brazil, in 2020. He is currently pursuing the M.S. degree in electrical engineering with the Universidade Federal do Rio Grande do Sul (UFRGS), Porto Alegre, Brazil. He has over 10 years of experience in the industrial sector, focusing on the development and management of electrical engineering projects. He works as a Researcher of Innovation, Science and Technology at Instituto Hercilio Randon, located in Farroupilha, RS, Brazil. His current research interests include electric mobility technologies, specifically the development of axial flux electric machines and static converters for electric and hybrid vehicles to promote alternative propulsion solutions.

Augusto Rodrigues Rauber received his degree of Electrical Engineer from the Universidade Regional Integrada do Alto Uruguai e das Missoes (URI), Santo Angelo, RS, Brazil, in 2023. He is currently pursuing a Master's degree in electromagnetic devices at the Universidade Federal do Rio Grande do Sul (UFRGS), Porto Alegre, RS, Brazil, with expected completion in 2026. He is currently working as a Science and Technology Analyst at Instituto Hercilio Randon, Farroupilha, RS, Brazil. His current research interests include electromagnetic devices and related technologies.

Leonardo Roso Colpo received his degree in Mechanical Engineering from Universidade Federal de Santa Maria (UFSM), Santa Maria, RS, Brazil, in 2019 and received the master's degree at the same institution in 2021. He's currently at the last year of his PhD Degree, focusing on vehicle dynamics, vibration control, and human biodynamics. His research activities involve modeling and simulation of full-vehicle systems, development of biodynamic human models, and the application of machine learning techniques, such as artificial neural networks, for vibration attenuation and comfort optimization. He has published works in national and international conferences addressing advanced control strategies and vibration analysis applied to automotive systems. He works as a Researcher of Innovation, Science and Technology at Instituto Hercilio Randon, located in Farroupilha, RS, Brazil. Also, it's a member of the technical committee of Baja Sae Brasil National and Regional student competitions.

Felipe Bruschi was born in Bento Goncalves, RS, Brazil, in 1999. He received the B.S. degree in electrical engineering from the Federal University of Santa Maria (UFSM), Santa Maria, RS, Brazil, in 2024. His major field of study was electrical engineering, with specialization in power electronics. During his undergraduate studies, he completed an international academic exchange at the Universita di Parma, Parma, Italy, from 2022 to 2023, through a sandwich program associated with UFSM. He is currently a Science and Technology Analyst at Instituto Hercilio Randon, Farroupilha, RS, Brazil. His professional experience includes research, development, and normative testing activities, as well as hardware development for industrial embedded systems and motor drives, working from system concept to final delivery. He has also participated in activities of an IEEE Student Branch. His current and previous research interests include power electronics, electric machines, traction inverters, vehicle electrification, embedded hardware for industrial applications, normative testing, and test benches.

Diorge Alex Bao Zambra was born in Ijui, RS, Brazil, in 1980. He received the B.S. degree in Electrical Engineering from the Universidade Regional do Noroeste do Estado do Rio Grande do Sul, Ijui, Brazil, in 2003, and the M.Sc. and Ph.D. degrees in Electrical Engineering from the Universidade Federal de Santa Maria, Santa Maria, Brazil, in 2006 and 2010, respectively. He also received a postgraduate certificate in University Management from the Universidade de Caxias do Sul, Caxias do Sul, Brazil, in 2014. He has held academic positions in both public and private institutions. From 2009 to 2017, he was with the Universidade de Caxias do Sul, where he taught in the undergraduate Electrical Engineering Program and in the Professional Master's Program in Mechanical Engineering. Since 2018, he has been with the Universidade Federal do Rio Grande do Sul, Tramandai, Brazil, where he is a professor in the Energy Management Engineering Program. He is currently a Postdoctoral Research Fellow at the Instituto Hercilio Randon, working on the development of power inverters for automotive applications. His research interests include power electronics, particularly inverter design, modulation techniques, and control strategies applied to industrial, automotive, and alternative energy generation systems.